Cite article as: S. K. Dayalan, Narayan K. Sundaram, Partial slip contact of a rigid pin and a linear viscoelastic plate *International Journal of Solids and Structures* **100-101**(2016) 319-331 http://dx.doi.org/10.1016/j.ijsolstr.2016.09.001

Partial slip contact of a rigid pin and a linear viscoelastic plate

Satish Kumar Dayalan, Narayan K. Sundaram*

Department of Civil Engineering, Indian Institute of Science, Bangalore, India 560012

Abstract

This paper analyzes partial slip contact problems in the theory of linear viscoelasticity under a wide variety of loading conditions, including cyclic (fretting) loads, using a semi-analytical method. Such problems arise in applications like metal-polymer contacts in orthopedic implants. By using viscoelastic analogues of Green's functions, the governing equations for viscoelastic partial-slip contact are formulated as a pair of coupled Singular Integral Equations (SIEs) for a conforming (pin-plate) geometry. The formulation is entirely in the time-domain, avoiding Laplace transforms. Both Coulomb and hysteretic effects are considered, and arbitrary load histories, including bidirectional pin loads and remote plate stresses, are allowed. Moreover, the contact patch is allowed to advance and recede with no restrictions. Viscoelasticity necessitates the application of the stick-zone boundary condition in convolved form, and also introduces additional convolved gap terms in the governing equations, which are not present in the elastic case. Transient as well as steady-state contact tractions are studied under monotonic ramp-hold, unload-reload, cyclic bidirectional (fretting) and remote plate loading for a three-element solid. The contact size, stick-zone size, indenter approach, Coulomb energy dissipation and surface hoop stresses are tracked during fretting.

Viscoelastic fretting contacts differ from their elastic counterparts in notable ways. While they shakedown just like their elastic counterparts, the number of cycles to attain shakedown states is strongly dependent on the ratio of the load cycle time to the relaxation time. Steady-state cyclic bulk hysteretic energy dissipation typically dominates the cyclic Coulomb dissipation, with a more pronounced difference at slower load cycling. However, despite this, it is essential to include Coulomb friction to obtain accurate contact stresses. Moreover, while viscoelastic steady-state tractions agree very well with the elastic tractions using the steady-state shear modulus in load-hold analyses, viscoelastic fretting tractions in shakedown differ considerably from their elastic counterparts. Additionally, an approximate elastic analysis misidentifies the edge of contact by as many as 7 degrees in fretting, showing the importance of viscoelastic contact analysis. The SIE method is not restricted to simple viscoelastic networks and is tested on a 12-element solid with very long time scales. In such cases, the material is effectively always in a transient state, with no steady edge-of-contact. This has implications for fretting crack nucleation.

Keywords: Contact, Viscoelasticity, Friction, Integral Equation, Metal-polymer contact, Pin-loaded connection, Dissipation

1. Introduction

The contact of a viscoelastic polymer with a counterbody made of a much stiffer material has drawn considerable attention because of its importance in applications like rubber tires. There is a significant body of work focused on the frictional characteristics of soft elastomers like rubber (Grosch, 1963; Persson, 2001; Carbone and Putignano, 2013). Friction in such materials is attributed to bulk hysteretic losses, and typically investigated under conditions of rolling or sliding.

Early analytical work in viscoelastic contacts includes the solution of the Hertz-type problem with a monotonically increasing contact area (Lee and Radok, 1960), its extensions to non-monotonic cases (Hunter, 1960; Ting, 1966; Graham, 1967), and viscoelastic rolling contacts (Hunter, 1961; Morland, 1968). In plane-strain viscoelastic contacts, an extension of the Kolosov-Muskhelishvili method of linear elasticity has been used to solve both frictionless (Golden and Graham, 1988) and Coulomb limiting-friction problems (Goryacheva, 2008). More recent analytical / semi-analytical work has addressed such problems as adhesion in viscoelasticity (Hui et al., 1998) and the contact of viscoelastic bodies with hard, rough surfaces (Persson et al., 2004; Chen et al., 2011). However, the Coulomb partial slip regime in viscoelastic contacts has received much less attention. In partial slip contact, global relative tangential motion (sliding) does not occur. Instead, the contact consists of slip zones, where local relative tangential motion does occur, and stick zones, where no relative tangential motion occurs (Johnson, 1987).

Partial slip viscoelastic contacts arise in applications like orthopedic implants, which involve contact between a metal and a polymer (Duisabeau et al., 2004). The metal is typically austenitic stainless-steel or a titanium alloy like Ti6-Al-4V, while the polymer is usually Polymethyl Methacrylate (PMMA) or an Ultra-high Molecular Weight Polyethylene (UHMWPE) (Geringer et al., 2005). The failure of these implants is understood to be driven by a complex, contact-driven process known as fretting corrosion (Tritschler et al., 1999; Geringer et al., 2005), in which the deleterious effect of a corrosive environment enhances fretting (Higham et al., 1978). Cyclic loading of such contacts occurs during routine use of the limbs, e.g. while walking (Kim et al., 2013). Either the metal or the polymer may undergo damage, with wear debris from both materials reported in experiments (Tritschler et al., 1999). In metal-on-metal fretting, it is known that high-fidelity analysis of the edge-of-contact stress is an essential ingredient of fretting crack nucleation models (Fellows et al., 1995; McVeigh et al., 1999). This involves accurate modeling of partial slip contacts and tracking of the contact stress history during cyclic loading. Accurate contact stress analysis might be expected to provide similar insights into metal-polymer fretting.

The introduction of partial slip complicates contact problems in elasticity as well as in viscoelasticity. This is because of the history dependent nature of partial slip contacts, which makes their analysis inherently incremental, and coupling between pressure and shear tractions in the

*Assistant Professor; Corresponding author.
Email address: nsundaram@civil.iisc.ernet.in (Narayan K. Sundaram)

governing equations. An early partial slip solution in linear viscoelasticity was obtained by Goryacheva (1973) for rolling of a viscoelastic cylinder on a halfspace of a similarly viscoelastic material[1]. Other Coulomb frictional viscoelastic solutions include the rolling contact of layered cylinders (Kalker, 1991) and a cylinder rolling on a viscoelastic layer atop an elastic halfspace (Goryacheva and Sadeghi, 1995). The assumption of material similarity in Goryacheva (1973) or the Goodman approximation (Goodman, 1962) in Goryacheva and Sadeghi (1995) is analytically helpful because it eliminates coupling between the pressure and shear tractions. However, these assumptions are inapplicable to metal-polymer contacts, where the counterbody is much stiffer. Moreover, partial slip fretting contacts may be subject to very complex load histories. Under such conditions, it is almost impossible to obtain closed-form solutions. However, formulating the governing equations of contact as Singular Integral Equations (SIEs) leads to a fast, semi-analytical method to solve these problems.

The present work builds an accurate SIE-based model for partial slip viscoelastic contacts in monotonic and cyclic loading, thereby accounting for both Coulomb and hysteretic effects. The starting point is a viscoelastic analogue of the elastic Green's functions. Since metals are typically much stiffer than polymers, it is a good assumption to treat the metal as a rigid body.

The conforming (pin-plate) geometry is chosen for our work because it has the advantage of allowing calculation of indenter approach, and thus various energy dissipation estimates, in plane strain viscoelasticity. Furthermore, the implant contact geometry is typically of a conforming type. Conforming contacts also have the advantage of including halfspace contacts as a limiting case. Conforming elastic contacts have been studied extensively in both receding and advancing contact regimes (Gladwell, 1980; To and He, 2008). Two frictionless conforming contact solutions are known in linear viscoelasticity, both in the receding (rather than advancing) contact regime. Margetson and Morland (1970) considered the problem of separation of an inclusion from a viscoelastic plate in uniaxial loading. Subsequently, Golden and Graham (2001) considered the same problem with biaxial loading.

2. Formulation

2.1. Creep and relaxation functions of a linear viscoelastic solid

The shear relaxation modulus of a linear viscoelastic solid is represented by (Golden and Graham, 1988) (Fig. 1)

$$\boldsymbol{G}(t) = G_\infty + \sum_{i=1}^{n} G_i \exp(-\frac{t}{\tau_i}) = G_0 - \sum_{i=1}^{n} G_i(1 - \exp(-\frac{t}{\tau_i})) \tag{2.1}$$

where G_0 is the instantaneous modulus, G_i the shear moduli of the network spring elements, τ_r are relaxation time constants and G_∞ is the modulus at $t = \infty$. Similarly, the creep response is

[1]This is the viscoelastic analogue of Carter's problem (Barber, 2010)

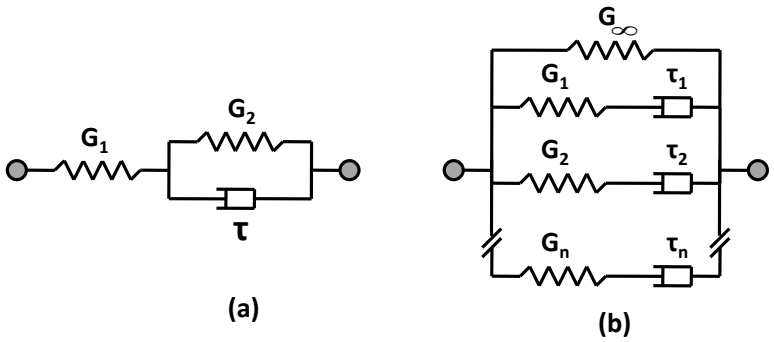

Figure 1: (a) Three-element delayed elastic solid and (b) generalized Maxwell model

characterized by

$$\boldsymbol{J}(t) = J_\infty - \sum_{r=1}^{n} J_r \exp(-\frac{t}{\lambda_r}) = J_0 + \sum_{r=1}^{n} J_r(1 - \exp(-\frac{t}{\lambda_r})) \tag{2.2}$$

where J_r and λ_r represent, respectively, the compliances of the springs and retardation time constants.

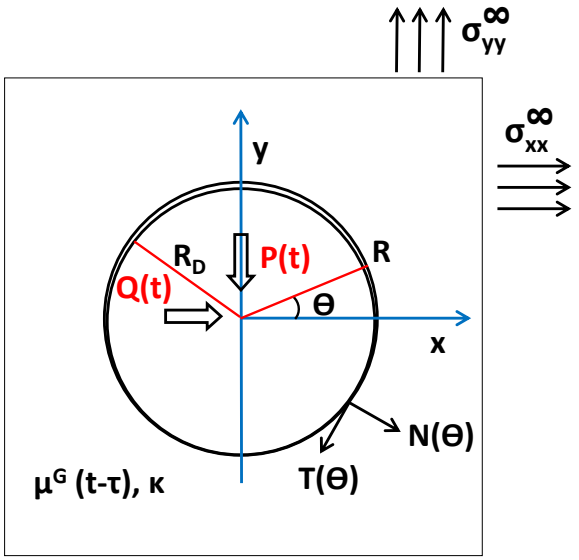

Figure 2: Schematic of a rigid pin in partial-slip contact with a viscoelastic plate. $R_D < R$ and the contact may advance as well as recede during loading.

2.2. Governing equations of the contact problem

A general way to formulate contact problems for linear media is to use appropriate Green's functions. These are typically surface displacements produced by point normal and tangential loads acting on the boundary of the domain. We first derive a viscoelastic analogue of the elastic

Green's functions for the plate, by using an extension of the Kolosov-Muskhelishivili formulation for viscoelastic materials (see Appendix A).

Then, let $R_D < R$ be the radius of the rigid pin. In the reference state, the pin rests on the plate as shown in Fig. 2. If the pin is rotated by a small amount C_ω, and pressed into the viscoelastic plate by a rigid displacement $\overline{V} = (C_{0x}, -\Delta)$, the gap function $h_d(\theta, t)$ is

$$h_d(\theta, t) = (R - R_D)(1 + \sin(\theta)) - C_{0x}(t)\cos(\theta) + \Delta(t)\sin(\theta) \tag{2.3}$$

The overclosures thus produced must be relieved at every point by displacements in the viscoelastic plate so that the new gap equation is

$$h(\theta, t) + (R_D - R)(1 + \sin(\theta)) + C_{0x}\cos(\theta) - \Delta\sin(\theta) - \tilde{v}_r^\infty = \tilde{v}_r^p + \tilde{v}_r^q \tag{2.4}$$

Here $\tilde{v}_r^p$ and $\tilde{v}_r^q$ are, respectively, the radial surface displacements of the plate due to normal and shear tractions, and $\tilde{v}_r^\infty$ is the radial surface displacement caused by remote stresses applied to the plate. Clearly, the gap function $h(\theta, t) = 0$ inside the contact. Similarly, the slip function $s(\theta, t)$ is related to the traction-induced tangential surface displacements $\tilde{v}_\theta^p, \tilde{v}_\theta^q$ of the plate

$$-s(\theta, t) + C_\omega(t)R - \Delta(t)\cos(\theta) - C_{0x}(t)\sin(\theta) - \tilde{v}_\theta^\infty = \tilde{v}_\theta^p + \tilde{v}_\theta^q \tag{2.5}$$

Using the Boltzmann Superposition Principle and the linearity of the medium (Golden and Graham, 1988; Sternberg and Al-Khozaie, 1964), contributions to the surface displacement from individual point loads N, T (Eqs. (A.9a), (A.9b)) may be distributed to arrive at the overall surface displacement due to the contact tractions. For instance, using Eq. (A.9a), $\tilde{v}_r^p$, the radial surface displacement due to the pressure tractions is (see Appendix A for definitions)

$$\tilde{v}_r^p(\theta, t) = \frac{R}{4\pi}\int_\alpha^\beta (\kappa'' S(\theta, \xi)A(\theta, \xi) - \kappa' C(\theta, \xi)L(\theta, \xi)) \left(\int_{0^-}^{t^+} \boldsymbol{\gamma^g}(t - \tau)N(\xi, \tau)d\tau\right) d\xi \tag{2.6}$$

In an analogous manner to the elastic problem (Sundaram and Farris, 2010a), the $L \equiv \log(2 - 2\cos(\theta - \xi))$ kernel in the displacements in Eq. (2.6) causes analytical difficulties if one attempts to use terms like $\tilde{v}_r^p(\theta, t)$ unmodified. It is possible to overcome this issue as in the elastic case (Sundaram and Farris, 2010b), by applying a suitable (linear) matrix differential operator $[\boldsymbol{\partial_\theta}]$ to the displacements produced by point loads *prior* to distributing the loads, i.e. one considers

$$[\boldsymbol{\partial_\theta}] \begin{Bmatrix} \tilde{v}_r^p(\theta, t) + \tilde{v}_r^q(\theta, t) \\ \tilde{v}_\theta^p(\theta, t) + \tilde{v}_\theta^q(\theta, t) \end{Bmatrix} = R\int_\alpha^\beta \begin{bmatrix} 1 & \dfrac{\partial}{\partial\theta} \\ -\dfrac{\partial}{\partial\theta} & 1 \end{bmatrix} \begin{Bmatrix} \tilde{v}_r^N(\xi, \theta, t) + \tilde{v}_r^T(\xi, \theta, t) \\ \tilde{v}_\theta^N(\xi, \theta, t) + \tilde{v}_\theta^T(\xi, \theta, t) \end{Bmatrix} d\xi \tag{2.7}$$

It is easily seen that this procedure eliminates the problematic logarithmic cosine terms in Eq. (2.6).

Similarly, when the operator $[\boldsymbol{\partial_\theta}]$ is applied to the surface displacements expressed in terms of gap and slip inside the contact (Eqs. (2.4),(2.5)), it eliminates the approach terms $\Delta(t)$ and $C_{0x}(t)$.[2] Thus, we have

$$[\boldsymbol{\partial_\theta}] \begin{Bmatrix} \tilde{v}_r^p(\theta,t) + \tilde{v}_r^q(\theta,t) \\ \tilde{v}_\theta^p(\theta,t) + \tilde{v}_\theta^q(\theta,t) \end{Bmatrix} = \begin{Bmatrix} h(\theta,t) + (R_D - R)(1+\sin(\theta)) - s'(\theta,t) - G_s^*(\theta,t) \\ -h'(\theta,t) + C_\omega R - s(\theta,t) + (R - R_D)\cos(\theta) - G_p^*(\theta,t) \end{Bmatrix} \tag{2.8}$$

where the remote stress dependent functions $G_p^*(\theta,t)$ and $G_s^*(\theta,t)$ are defined as

$$\tilde{v}_r^\infty + \tilde{v}_\theta^{'\infty} \equiv G_s^*(\theta,t) = \frac{R\kappa^{'}}{2}\left[\frac{\mathscr{A}^*}{2} - \mathscr{D}^*\cos(2\theta)\right] \tag{2.9a}$$

$$\tilde{v}_\theta^\infty - \tilde{v}_r^{'\infty} \equiv G_p^*(\theta,t) = \frac{R\kappa^{'}}{2}\mathscr{D}^*\sin(2\theta) \tag{2.9b}$$

and the surface displacements produced by the remote stresses are given by Eq. (A.10). Equating the right-hand sides of Eqs. (2.7), (2.8) and simplifying, one obtains the following pair of governing SIEs for the rigid on viscoelastic contact problem, with the tractions appearing in $\boldsymbol{\gamma^g}$-convolved form as $N^* \equiv \boldsymbol{\gamma^g} * N(\theta,t)$ and $T^* \equiv \boldsymbol{\gamma^g} * T(\theta,t)$

$$\begin{aligned} h(\theta,t) + (R_D - R)(1+\sin\theta) - s'(\theta,t) - G_s^*(\theta,t) = \frac{R}{4\pi}\Bigg[\kappa' \int_\alpha^\beta \cot\left(\frac{\theta-\xi}{2}\right) T^*(\xi,t)d\xi \\ -\pi\kappa'' N^*(\theta,t) - \kappa\int_\alpha^\beta \sin(\theta-\xi)T^*(\xi,t)d\xi + \kappa'\int_\alpha^\beta N^*(\xi,t)d\xi + \kappa\int_\alpha^\beta \cos(\theta-\xi)N^*(\xi,t)d\xi\Bigg] \end{aligned} \tag{2.10}$$

$$\begin{aligned} C_\omega(t)R - s(\theta,t) - h'(\theta,t) + (R-R_D)\cos\theta - G_p^*(\theta,t) = \frac{R}{4\pi}\Bigg[-\kappa\int_\alpha^\beta \cos(\theta-\xi)T^*(\xi,t)d\xi \\ -\kappa'\int_\alpha^\beta T^*(\xi,t)d\xi + \pi\kappa'' T^*(\theta,t) + \kappa'\int_\alpha^\beta \cot\left(\frac{\theta-\xi}{2}\right) N^*(\xi,t)d\xi - \kappa\int_\alpha^\beta \sin(\theta-\xi)N^*(\xi,t)d\xi\Bigg] \end{aligned} \tag{2.11}$$

Here $h(\theta,t), h'(\theta,t)$ vanish inside the contact, which extends from $\theta = \alpha$ to $\theta = \beta$. It is easy to check that when the plate is elastic, $\boldsymbol{\gamma^g}(t-\tau) = \frac{1}{G}\delta(t-\tau)$, $N^* = N/G$, $T^* = T/G$, $\mathscr{A}^* = \mathscr{A}$/G, $\mathscr{D}^* = \mathscr{D}$/G and the equations reduce to the SIE governing the rigid on elastic contact in Sundaram and Farris (2010a). Additionally, no relative tangential motion occurs in the stick zone, i.e.

$$s(\theta,t) = s(\theta,t-\Delta t) \quad \forall\theta \in \text{ stick}, \Delta t > 0 \tag{2.12}$$

[2] It is not sufficient for the linear operator to eliminate L; it must also eliminate the approach terms. $[\boldsymbol{\partial_\theta}]$ is the simplest linear operator that has this property

In the slip zones, the shear traction is obtained by applying the local version of Coulomb's law

$$T(\theta,t) = \text{sign}\,(s(\theta,t) - s(\theta,t-\Delta t))\mu N(\theta,t) \quad \forall\theta \in \text{ slip} \tag{2.13}$$

It should be noted that Eqs. (2.10),(2.11) are exact in the present framework (plane-strain, linear viscoelastic material with constant κ, rigid pin).

3. Inversion and Solution

It is difficult to solve the coupled system of SIEs (2.10), (2.11) if the convolved pressure and shear, N^* and T^*, are treated as the primary unknowns. This is because N^* and T^* are analytically very different from $N(\theta)$ and $T(\theta)$. For instance, while $N(\theta) = 0$ at the ends of contact, this is not necessarily true for N^*. Similarly, while $T(\theta)$ can be expressed as a sum of functions, one of which vanishes at the ends of contact, and the other at the ends of the stick-zone, i.e.,

$$T(\theta) = \mu f(\theta)N(\theta) - T_q(\theta) \tag{3.1}$$

the convolved function T^* cannot be decomposed in this way. The non-vanishing of N^* and T^* at the ends of contact is problematic from the point of view of the theory of SIE, which demands that solutions bounded at the ends of the contact domain must also go to zero there (Muskhelishvili, 1992). To circumvent this problem, and use standard SIE techniques, one works with unconvolved tractions by applying the inverse operator $\boldsymbol{\mu^g}$ to Eqs. (2.10), (2.11), giving

$$h_*(\theta,t) + (R_D - R)(1+\sin\theta)\boldsymbol{G}(t) - s'_*(\theta,t) - G_s(\theta,t) = \frac{R}{4\pi}\left[\kappa'\int_\alpha^\beta \cot\left(\frac{\theta-\xi}{2}\right)T(\xi,t)d\xi\right.$$
$$\left. -\pi\kappa'' N(\theta,t) - \kappa\int_\alpha^\beta \sin(\theta-\xi)T(\xi,t)d\xi + \kappa'\int_\alpha^\beta N(\xi,t)d\xi + \kappa\int_\alpha^\beta \cos(\theta-\xi)N(\xi,t)d\xi\right]$$
$$C_{\omega*}(t)R - s_*(\theta,t) - h'_*(\theta,t) + (R-R_D)\cos\theta\,\boldsymbol{G}(t) - G_p(\theta,t) = \frac{R}{4\pi}\left[-\kappa\int_\alpha^\beta \cos(\theta-\xi)T(\xi,t)d\xi\right. \tag{3.2}$$
$$\left. -\kappa'\int_\alpha^\beta T(\xi,t)d\xi + \pi\kappa'' T(\theta,t) + \kappa'\int_\alpha^\beta \cot\left(\frac{\theta-\xi}{2}\right)N(\xi,t)d\xi - \kappa\int_\alpha^\beta \sin(\theta-\xi)N(\xi,t)d\xi\right] \tag{3.3}$$

The asterisks in subscripts in Eqs. (3.2), (3.3) denotes quantities convolved with $\boldsymbol{\mu^g}$. Notice that the slip function $s(\theta,t)$ and its spatial derivative $s'(\theta,t)$ now appear in convolved form. *Importantly, the convolved forms of the gap h_* and gap-gradient h'_* appear in these equations, and are non-zero, even though $h = 0$ inside the contact at any time.* This also shows why it is essential to retain h, h' in Eqs. (2.10),(2.11).

In convolved form, the stick zone boundary condition Eq. (2.12) is written as

$$\int_0^t \boldsymbol{\gamma^g}(t-\tau)s_*(\theta,\tau)d\tau = \int_0^{t-\Delta t} \boldsymbol{\gamma^g}(t-\Delta t-\tau)s_*(\theta,\tau)d\tau \quad \forall\theta \in \text{ stick} \tag{3.4}$$

Eq. (3.4) shows that the stick-zone kinematic boundary condition (2.12) does not, in general, imply that $s_*(\theta,t) = s_*(\theta,t-\Delta t)$. The unknown tractions must also integrate to the applied vertical and horizontal loads $P(t), Q(t)$

$$\int_\alpha^\beta \left(T(\theta,t)\cos\theta - N(\theta,t)\sin\theta\right)d\theta = \frac{P(t)}{R} \tag{3.5a}$$

$$\int_\alpha^\beta \left(T(\theta,t)\sin\theta + N(\theta,t)\cos\theta\right)d\theta = \frac{Q(t)}{R} \tag{3.5b}$$

Eqs. (3.2), (3.3), (3.4), (3.5) and (2.13) are then of a form that allow one to solve for $N(\theta), T(\theta)$ using the numerical method in Sundaram and Farris (2010a). Details of the method may be found there, but the procedure involves reduction of the equations to Cauchy form (kernel $1/(x-s)$) with a change of variables, and additive decomposition of the unknown tractions into a bounded term and singular terms of a suitable form. These equations are then solved using Newton-Raphson iteration for a set of contact and stick-zone ends $\alpha, \beta, \alpha_s, \beta_s$, subject to satisfaction of the global equilibrium conditions Eqs. (3.5) and vanishing of the coefficients of the added singular terms.

The history effects necessitate calculation and storage of s_*, s'_*, h_* and h'_* on an arc which is a super-set of all potential contact regions. For example, inside the contact, $h_*(\theta,t)$ is calculated from

$$h_*(\theta,t) = \int_{0^-}^{t^+} \boldsymbol{\mu^g}(t-\tau)h(\theta,\tau)d\tau = \boldsymbol{G}(0)h(\theta,t) - \int_0^t \left(\frac{d}{d\tau}\boldsymbol{G}(t-\tau)\right)h(\theta,\tau)d\tau \tag{3.6}$$

and the gap *history* $h(\theta,t)$. Outside the contact, one solves for $h_*(\theta)$ using the known $N(\theta), T(\theta)$

$$\begin{aligned} h_*+h''_* = \boldsymbol{G}(t)(R-R_D)+\frac{R\kappa'}{2}\left[\frac{\mathscr{A}}{2} - 3\mathscr{D}\cos(2\theta)\right]+\frac{R}{4\pi}\left[\kappa'\int_\alpha^\beta N(\xi)d\xi + 2\kappa\int_\alpha^\beta \cos(\theta-\xi)N(\xi)d\xi\right. \\ \left. -\kappa'\int_\alpha^\beta \cot\left(\frac{\theta-\xi}{2}\right)N'(\xi)d\xi + \kappa'\int_\alpha^\beta \cot\left(\frac{\theta-\xi}{2}\right)T(\xi)d\xi - 2\kappa\int_\alpha^\beta \sin(\theta-\xi)T(\xi)d\xi\right] \end{aligned} \tag{3.7}$$

4. Results

The formulation and solution scheme discussed above are valid for any linear viscoelastic material with constant κ. Most of the results in this paper are for a three-element delayed-elastic solid (with one characteristic τ, see Fig. 1a). Results for a more representative generalized Maxwell

network with multiple characteristic times (Fig. 1b), are shown in a later section. For the three-element solid, $G_1 = G_2 = 1.37785 \times 10^5$ psi giving $G_0/G_\infty = 2.0$; $\kappa = 1.4$ and relaxation time $\tau = 5$s.

For the purpose of simplicity, we consider partial slip problems with the pin prevented from rotating, i.e. $C_w = 0$. It is helpful to introduce a non-dimensionalized loading parameter $L_p = (R - R_D)/(P\beta^*)$ where β^* is defined in terms of the instantaneous modulus as $\beta^* = (\kappa+1)/2G_0$. A smaller value of L_p represents a geometrically more conforming contact.[3]

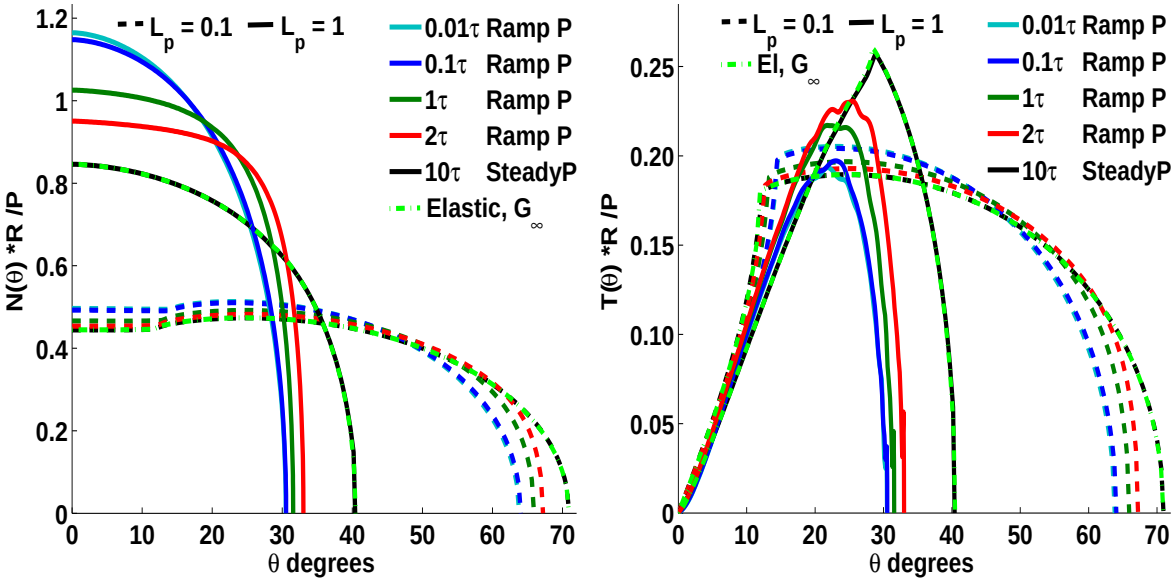

(a) (b)

Figure 3: Pressure (a) and shear (b) tractions for ramp-hold P loading at different loading rates. The dashed lines are tractions at $L_p = 0.1$, and the solid lines at $L_p = 1$. The tractions become steady after holding P beyond $t = 10\tau$. The steady-state tractions agree very well with the elastic traction using $G = G_\infty$ (green dotted line). The coefficient of friction $\mu = 0.40$ in all cases. Note that the contact tractions are symmetric in P-only analysis, and the tractions are shown over half the contact only. The mid-point of such contacts is at $\theta = -90°$ in the non-symmetrized (global) coordinate system in Fig.2

4.1. Monotonic load-hold analysis in partial slip

The simplest load path consists of two steps: A monotonically increasing ramp vertical (P) load applied over a time t_P in the first step, followed by a second step in which P is held constant. Fig. 3(a) shows partial-slip pressure tractions for a ramp-hold P load for two representative values of L_p, 0.1 and 1.0. Four different values of t_P are chosen, namely $0.01\tau, 0.1\tau, 1\tau, 2\tau$. A smaller value of t_P indicates a higher loading rate. The Coulomb friction coefficient $\mu = 0.40$ in all cases.

[3]It is also possible to use the steady state modulus G_∞ to define a slightly different parameter, L_p^*, so that $L_p^* = L_p G_\infty/G_0$.

Consider the solid lines in the figure, corresponding to $L_p = 1.0$. Very rapid loading ($t_P = 0.01\tau$) produces the stiffest response at the end of the P ramp, resulting in the highest peak pressure traction (N_{max}) and the smallest contact half-angle ϵ_0. Intermediate loading rates result in larger ϵ_0 and lower N_{max}. After the P ramp, the P-load is held constant for a time $t = 10\tau$. Irrespective of the loading rate, the steady-state $N(\theta)$ is the same (indicated by the solid black line in 3(a)).

At a smaller value of $L_p = 0.1$, representing geometrically more conforming contacts, wider contact half-angles ($\epsilon_0 = 65^\circ - 72^\circ$) and lower $N(\theta)$ are observed at the end of the P-ramp, indicated by the dashed lines in 3(a). Again, the steady-state $N(\theta)$ is the same in all cases, and corresponds to the lowest N_{max} and widest ϵ_0. Corresponding shear tractions for these analyses are shown in Fig. 3(b). Interestingly, at $L_p = 1$, the largest shear traction T_{max} occurs for the slowest loading rate (corresponding to the largest t_P) and decreases at lower t_P. There is a sharp change in gradient in all the $T(\theta)$ curves, demarcating the boundary between the (inner) stick and (outer) slip zones. The steady state $T(\theta)$ has the largest stick zone half-angle ρ_0. At lower values of L_p, the difference between the various $T(\theta)$ is not as significant as at the higher L_p. In this case, the corresponding ρ_0 are all in a narrow band of $12^\circ - 15^\circ$. Notably, the steady-state tractions agree very well with the elastic tractions using $G = G_\infty$.

On using a lower value of $\mu = 0.15$, it is seen that $N(\theta)$ does not change very much at high $L_p = 1.0$, but results in peak pressures that are about 20 percent higher at $L_p = 0.1$. On the other hand, the shear tractions for $\mu = 0.15$ are markedly lower at all values of t_P, L_p than when $\mu = 0.40$. In addition, the stick-zone sizes ρ_0 are much smaller; In particular, for $L_p = 0.1$, the size is no more than $< 5^\circ$, indicating that most of the contact is in slip.

4.2. Unloading and reloading in partial slip

It is illustrative to study the effect of history on unloading and reloading a partial slip viscoelastic contact. Figs. 4(a),4(b) show the pressure and shear tractions obtained on unloading and reloading from a steady state, in a three step analysis. In the first step, a ramp load P, corresponding to an initial $L_p = 0.25$ is applied and the contact allowed to attain near steady state by holding the load unchanged for $t = 10\tau$. In the second step, the contact is unloaded to a value of $0.2P$ over a step time 2.0τ. In the third step, the contact is immediately re-loaded back to P at the same rate.

The pressure tractions $N(\theta)$ show a clear difference during the unloading and the re-loading steps at the same applied load, with somewhat higher tractions and smaller ϵ_0 during re-loading. It should be noted that the traction at the end of the unloading step is roughly independent of the rate of unloading because of the receding nature of the contact. In fact, the convolved gap function $h_*(\theta)$ is unchanged inside each instantaneous contact patch $(\alpha(t), \beta(t))$ during unloading. However, during the reloading phase, the contact advances. The $h_*(\theta)$ during reloading is different from what it was during unloading, resulting in different tractions.

In contrast, Fig. 4(b) shows that the shear tractions are considerably different during unloading than during reloading, at identical load values. There is an initial reversal in the sign of $T(\theta)$ in the slip-zone at the beginning of the unloading step, subsequent to which the slip-zone grows at

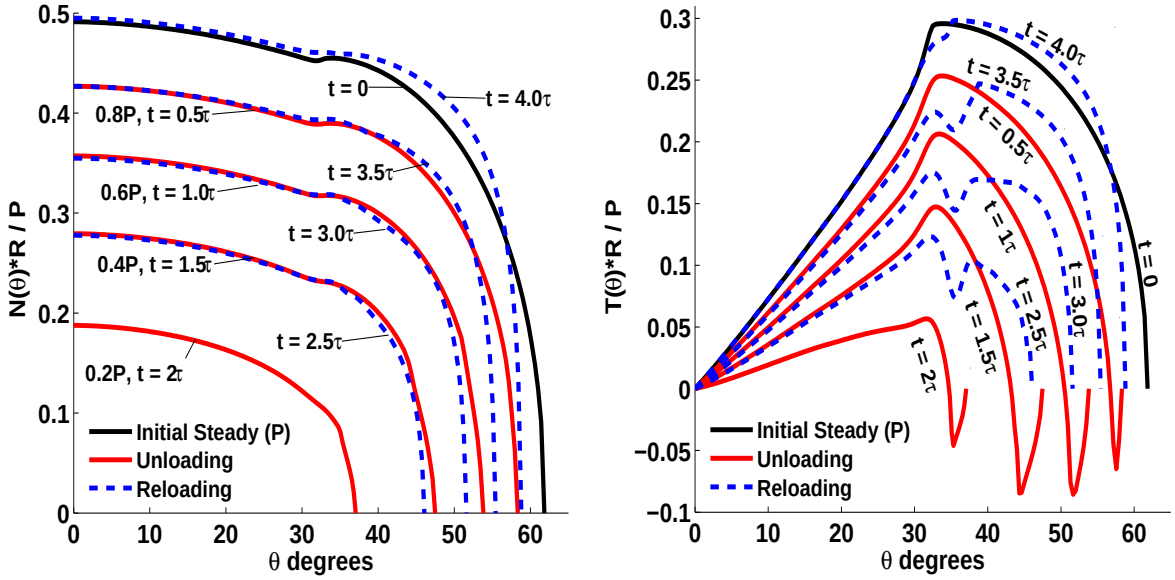

(a) (b)

Figure 4: Pressure (a) and shear (b) tractions for unloading (solid red lines) and reloading (dashed-lines) from an initially steady state ($t = 0$) (solid black line) with vertical load P corresponding to $L_p = 0.25$. The tractions are depicted at times $t = 0.5\tau, 1.0\tau, 1.5\tau$ and 2.0τ on unloading and at times $t = 2.5\tau, 3.0\tau, 3.5\tau$ and 4.0τ on reloading. The unloading and reloading rates have the same magnitude, $0.4P/\tau$. The Coulomb friction coefficient $\mu = 0.65$

the expense of a receding stick-zone. The contact also recedes during unloading. Thus, neither the Coulomb nor the viscous history effect influences the contact solution significantly during unloading. However, both history effects do influence the solution on reloading, producing very different $T(\theta)$.

4.3. Fretting-type (cyclic) loading in partial slip

The simplest fretting type load consists of ramp-hold application of a vertical P load, following by the cycling of the horizontal load Q as $+Q, -Q, +Q \ldots$ while keeping P constant. In addition to the normalized magnitude of Q, namely $\eta = Q/\mu P$, μ and L_p, the Q-load cycle-time ratio t_Q/τ is an important parameter in cyclic loading of viscoelastic contacts. The inverse of this parameter, is a measure of normalized loading frequency, since the characteristic frequency of the material $\omega \propto 1/\tau$, i.e., $t_Q/\tau = \omega/\omega_Q$ where ω_Q is the Q-load cycling frequency. Lower t_Q/τ correspond to high-frequency Q-load cycling, and vice-versa.

Fig. 5(a) shows the pressures $N(\theta)$ obtained for $\eta = 1, \mu = 0.40, L_p = 0.15$ and $t_Q = 4.0\tau$ with 8 Q reversals. This value of t_Q represents slow cycling. There is marked asymmetry in the $N(\theta)$ curves in the presence of the Q-loads. The most important observation is that the tractions $N(\theta)$ shakedown after a sufficient number of cycles, and subsequently oscillate between two different steady-states, one corresponding to the largest positive $+Q$ and the other to the most negative horizontal load $-Q$. Unlike elastic contacts, the number of cycles required to shakedown

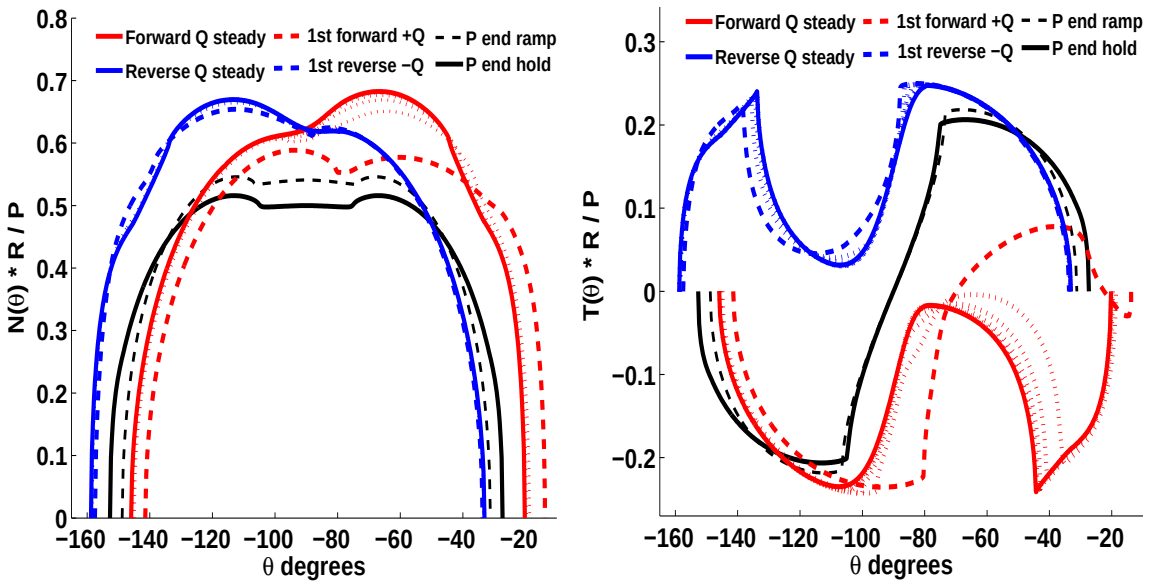

(a) (b)

Figure 5: Pressure(left) and shear(right) tractions in fretting type (cyclic) loading. The dotted lines indicate transient contact tractions at times obtained at times $t = 7\tau, 9\tau, \ldots$ when the Q-load is maximum or minimum. The contact tractions are symmetric about $\theta = -90°$ at the end of the P load-hold step. The Q-cycle time, $t_Q = 4.0\tau$, $L_p = 0.15$, $\mu = 0.4$

is not constant, but strongly influenced by t_Q. In this particular case, the tractions are almost indistinguishable after a period of 6 t_Q. Note that there is considerable difference between the $N(\theta)$ after the application of the first $+Q$, and the corresponding steady-state $N(\theta)$ at applied $+Q$. The significant shift in contact from the P only position, indicated by the black lines, is due to the conforming geometry. Some transient tractions, obtained at times $t = 7\tau, 9\tau, 11\tau \ldots$ corresponding to intermediate horizontal load-extrema, are depicted in the figure using dotted lines. It is seen that the highest peak pressure N_{max} is obtained in the steady-state(s).

The corresponding shear tractions $T(\theta)$ are shown in Fig. 5(b). Certain features of the $T(\theta)$ resemble elastic halfspace fretting tractions (Hills and Nowell, 1994); for example, there is a central stick-zone with slip zones on either side, and the sign of $T(\theta)$ in the two slip-zones is completely reversed in going from $+Q$ to $-Q$. Similarly, there is a shift in the mid-point of the contact as in elastic conforming contacts. Just like $N(\theta)$, the $T(\theta)$ also shakes down. The numerous cycles required to attain shakedown are, however, a result of the viscoelasticity. The intermediate $T(\theta)$ at $t = 7\tau, 9\tau, 11\tau \ldots$ are shown with dotted lines in the plot. It must be noted that if the Q-loading cycling sequence is $-Q, +Q, -Q, \ldots$, the obtained tractions would be a mirror-image of the tractions in Figs. 5(a),5(b).

Fig. 6(a) shows the evolution of contact half-angle ϵ_0 and stick-zone size ρ_0 during this analysis. ϵ_0 rises rapidly on applying the P-load[4] and increases again during the hold period as a result

[4]The slope $d\epsilon_0/dP$ is higher for smaller L_p and becomes infinite in the limiting case of $L_p = 0.0$

of the relaxation of $\boldsymbol{G}(t)$. The Q-cycling changes the ϵ_0 only by about 0.6° even though, as noted earlier, there is considerable shift in the position of the contact patch itself ($\sim 13^\circ$).

The time-evolution of the stick-zone size, ρ_0, is more interesting. Unlike ϵ_0, which is continuous, ρ_0 is a discontinuous function with numerous jumps, as indicated by the vertical line segments with arrows. Each jump corresponds to a reversal in the sign of $T(\theta)$ in one or both slip zones, either because of the change in sign of the applied dQ/dt (indicated by time markers $A_1, B_1, A_2 \ldots$), or at the beginning of application of the first $+Q$ load after applying P (time marker X). Notice that at each Q load reversal, the stick-zone size ρ_0 becomes almost equal to the contact size ϵ_0. On account of the dissimilarity of the materials, these values are theoretically never quite equal, just as in linear elasticity (Dundurs and Comninou, 1979). As the cycling is continued, the values of ϵ_0 and ρ_0 attain their 'shakedown' steady state values fairly quickly.

As noted earlier, the choice of conforming contact geometry allows determination of the approaches Δ and C_{0x}, shown in Fig. 6(b). The vertical approach Δ behaves like ϵ_0, initially increasing with time during the P ramp-hold step and eventually becoming nearly steady, with a small oscillation about a mean value as Q is cycled. In contrast, the horizontal approach C_{0x} changes dramatically during the Q cycling, with its largest positive values coinciding with times $A_1, A_2, \ldots$ and the most negative values coinciding with times $B_1, B_2, \ldots$. Like all other contact quantities, C_{0x} also eventually oscillates between two steady-state values.

The fretting analysis was repeated for different values of the load cycling time t_Q. Figs. 7(a),7(b) depict $N(\theta)$ and $T(\theta)$ for more rapid cycling using $t_Q = 1\tau$. The steady-state tractions are seen to be independent of the cycling time t_Q. However, the transient tractions for different values of t_Q can differ considerably. For instance, $T(\theta)$ at time A_1, corresponding to the end of application of $+Q$, has a much higher leading peak when $t_Q = 1\tau$ (Fig. 7(b)) than when $t_Q = 4\tau$ (Fig. 5(b)). Clearly, it requires more cycles to achieve shakedown at smaller values of t_Q/τ.

4.4. Surface hoop stress for fretting-type loads

Once the surface tractions $N(\theta)$ and $T(\theta)$ are obtained, the subsurface stress field can be calculated in a post-processing step by solving a pure traction b.v.p. This is done by calculating the stresses at any plate location (r, θ) resulting from point-loads N and T acting at arbitrary locations $\xi = \zeta$ on the edge of the hole ($r = R$), distributing these stress contributions over the entire contact and adding any remote stress contribution.

The hoop stress component $\tilde{\sigma}_{\theta\theta}$ at the edge of the hole is of particular interest as it 'opens' any edge crack nucleated on the surface. It is easy to show that the surface hoop stresses at location θ, caused by tractions $N(\theta)$ and $T(\theta)$ are given by the following integrals[5]

$$\tilde{\sigma}_{\theta\theta}(\theta)|_{N(\theta)} = \int_\alpha^\beta \frac{N(\zeta)}{\pi} \left[1 + \frac{2\kappa}{\kappa+1}\cos(\zeta - \theta)\right] d\zeta - N(\theta) \tag{4.1}$$

[5]The integral containing the $\cot$ term must, of course, be understood as a Cauchy principal value

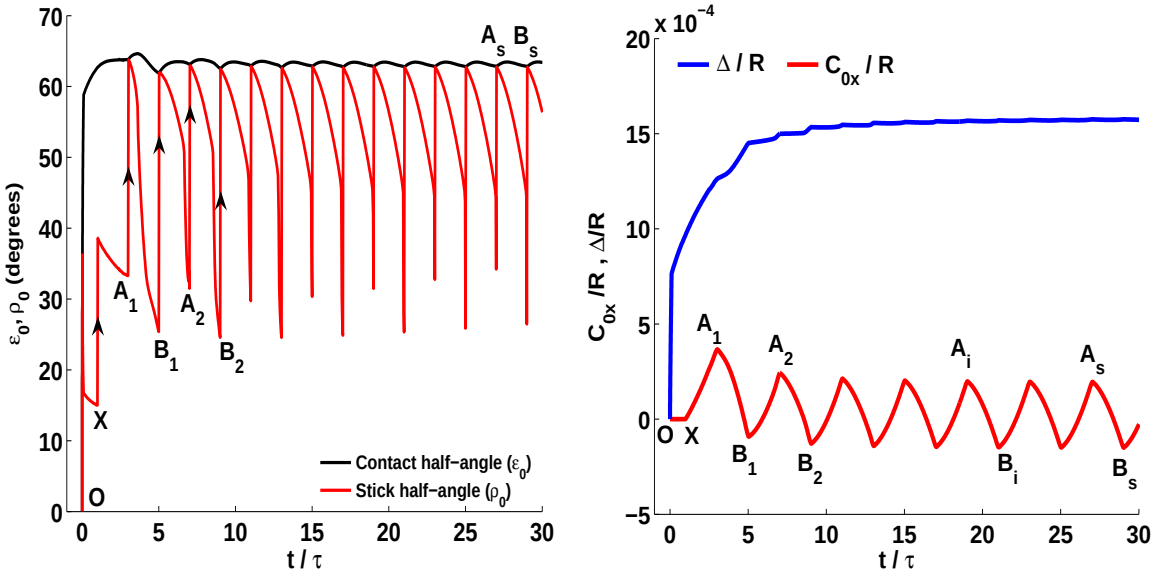

(a) (b)

Figure 6: (a) Evolution of contact and stick-zone half-angles and (b) Indenter vertical and horizontal approaches Δ, C_{0x} in fretting analysis for $t_Q = 4\tau$ (Normalized load frequency ω_Q/ω = 0.25). $L_p = 0.15$, $\eta = 1.0$ and $\mu = 0.4$. The stick-zone evolves in a discontinuous fashion (vertical segments in (a)), with the discontinuities representing changes in the sign of shear in the slip zone upon reversing the Q load. Time-markers $A_1, A_2, \ldots$ and $B_1, B_2, \ldots$ correspond to extremal $+Q$ and $-Q$ loads, respectively.

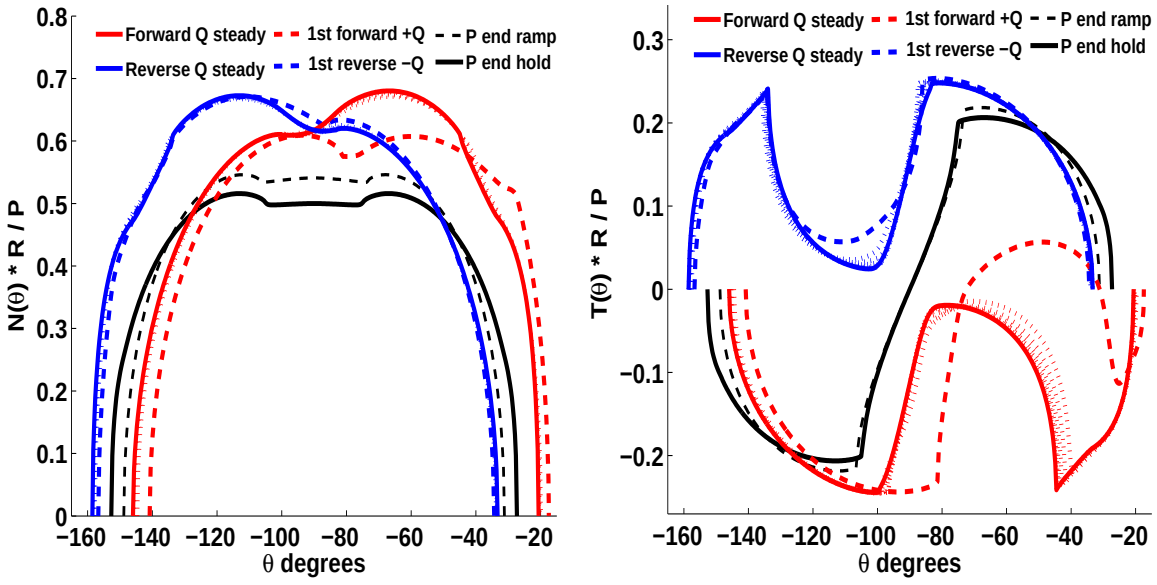

(a) (b)

Figure 7: Pressure(left) and shear(right) for fretting type (cyclic) loading with a more rapid Q-cycle time, $t_Q = 1.0\tau$ (ω_Q/ω = 1.0). $L_p = 0.15$, $\mu = 0.4$

$$\tilde{\sigma}_{\theta\theta}(\theta)|_{T(\theta)} = \int_{\alpha}^{\beta} \frac{T(\zeta)}{\pi} \left[\frac{2\kappa}{\kappa+1} \sin(\zeta-\theta) - \cot\left(\frac{\zeta-\theta}{2}\right) \right] d\zeta \tag{4.2}$$

In the presence of remote stresses, there is an additional term

$$\tilde{\sigma}_{\theta\theta}(\theta)|_{\sigma} = \sigma_{xx}^{\infty} + \sigma_{yy}^{\infty} - 2(\sigma_{xx}^{\infty} - \sigma_{yy}^{\infty}) \cos 2\theta = \mathscr{A} - 2\mathscr{D} \cos 2\theta \tag{4.3}$$

Notably, these equations are valid for both elastic and viscoelastic plates, since the stresses do not depend on $\boldsymbol{G}$, but only on κ. Clearly, the total $\tilde{\sigma}_{\theta\theta}(\theta) = \tilde{\sigma}_{\theta\theta}(\theta)|_{N(\theta)} + \tilde{\sigma}_{\theta\theta}(\theta)|_{T(\theta)} + \tilde{\sigma}_{\theta\theta}(\theta)|_{\sigma}$.

Fig. 8(a) shows a plot of representative $\tilde{\sigma}_{\theta\theta}(\theta)$ for fretting type loads with $L_p = 0.15$, $\eta = 1$, $\mu = 0.4$ and $t_Q = 2\tau$. After a sufficient number of Q-cycles, the stresses shakedown, and oscillate between two steady distributions, indicated by the solid blue line (-Q steady state) and the solid red line (+Q steady state). At the +Q steady state, the peak tensile stress occurs at the trailing edge of contact ($\theta = -146°$ and at the -Q steady state the peak tensile stress occurs at the edge on the other side of the contact ($\theta = -33°$). The two peak hoop stress values are the same because no remote plate stresses are present. Note that the steady state stresses are independent of the t_Q used. However, transient stress distributions, like the tractions, do depend on t_Q.

Fig. 8(b) shows the $\tilde{\sigma}_{\theta\theta}(\theta)$ for fretting-type loads with additional cyclic remote plate-stresses σ_{yy}^{∞} with $t_Q = 4\tau$. Both the Q-load and σ_{yy}^{∞} are cycled in phase, with σ_{yy}^{∞} varied from 0 to $0.2P/R$ in tension. The presence of the remote tension causes an asymmetry in the steady-state hoop stresses. The peak steady-state forward tensile hoop stress magnitude rises to $1.28P/R$ when compared to Fig. 8(a), while the peak steady-state reverse tensile hoop stress magnitude is slightly lower, at $0.85P/R$.

4.5. Coulomb and viscous energy dissipation in fretting

Two dissipative mechanisms operate in the viscoelastic contacts considered here: The Coulomb mechanism, which is entirely interfacial and restricted to the slip zones, and the hysteretic (bulk) dissipation due to viscoelasticity. In the absence of remote stresses, the external work input to the system W_{ext} is through the vertical load P(t) and horizontal load Q(t) only. The work input up to time t is given by

$$W_{ext} = \int P \; d\Delta + \int Q \; dC_{0x} \approx \sum_{i=1}^{M} \left(P_i \; \delta\Delta_i + Q_i \delta C_{0x,i} \right) \tag{4.4}$$

where the integral is replaced by a summation over all M increments in the analysis. Note that the integrands in Eq. (4.4) are always positive.

The Coulomb frictional energy W_c dissipated up to a given time t depends on the slip velocity

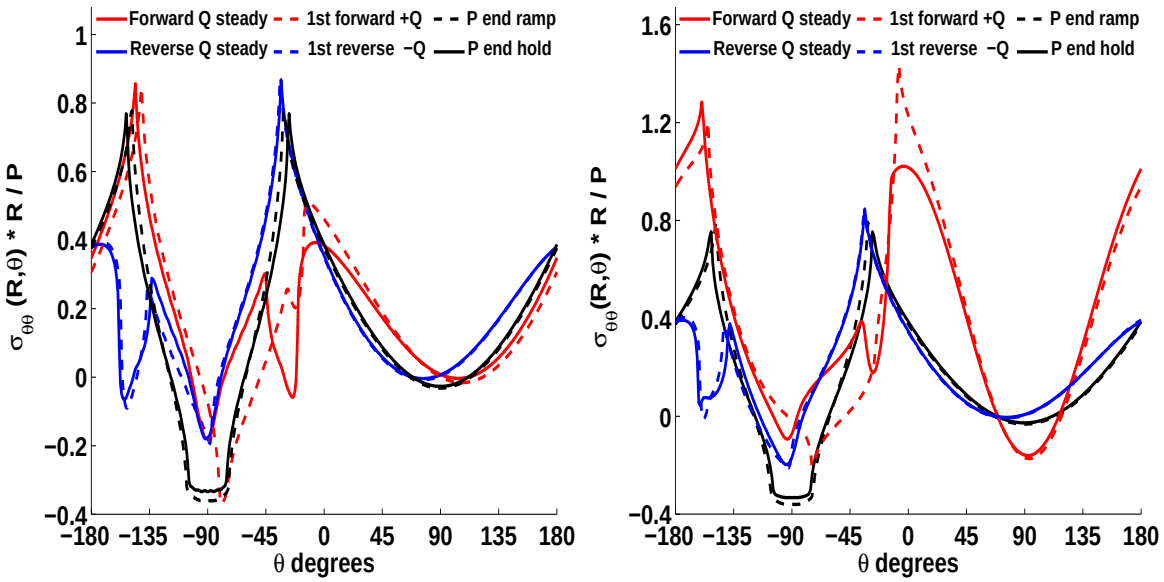

Figure 8: Hoop stress $\tilde{\sigma}_{\theta\theta}$ at the surface (r=R) for fretting type loads. (a) Fretting Q-load cycling only, $t_Q = 2\tau$. (b) In-phase cycling of fretting Q-load and a remote plate stress σ^{∞}_{yy} of magnitude varying from 0 to $0.2P/R$. $t_Q = 4\tau$.

$\dot{s}$ in the slip-zones and the tangential tractions, as[6]

$$W_c = R\int_0^t \left(\int_{S_L(t)} T(t,\theta)\dot{s}(t,\theta)d\theta\right)dt = R\sum_{i=1}^{M}\left(\int_{S_L(t)} T_i(\theta)\frac{\delta s(\theta)}{\delta t_i}d\theta\right)\delta t_i \qquad (4.5)$$

The inner integral is taken over the instantaneous slip region, $S_L(t)$. Since the tractions, approaches and slip histories are known from the analysis, both W_{ext} and W_c can be calculated using Eqs.(4.4) and (4.5).

Fig. 9(a) shows the Coulomb dissipation W_c, inputs from the loads W_P, W_Q and the total external work input, W_{ext} for the fretting analysis with $t_Q = 4\tau$ described in an earlier section. The dissipative nature of the system accounts for the fact that W_{ext} increases with time, on average.

The local decreases in W_Q (and W_{ext}) can be explained by the fact that the applied Q load decreases in magnitude during half of a load cycle, and increases in another half. In particular, it takes a value of 0 midway between times like $t = A_i$ and $t = B_i$. At these local minima, the power input due to Q (slope of the W_Q curve) is 0. While W_Q keeps increasing on average, the work input from the vertical load W_P is seen to become almost constant, with a slightly positive slope. This indicates that at steady state, most of the input power is supplied by the Q load. The Coulomb component W_c has a more gentle slope at large t, indicating that viscous losses eventually consume the largest share of input power.

[6]Because of the way the sign of $T(\theta)$ is chosen in Eq. (2.13), this integrand is always positive

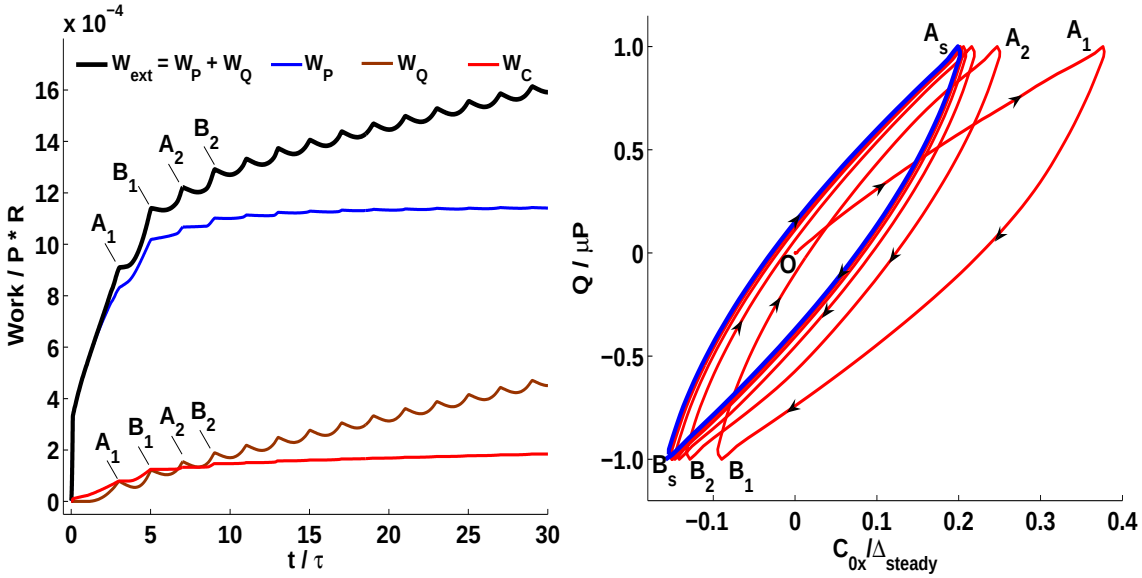

(a) (b)

Figure 9: (a) Work input and Coulomb frictional energy dissipation and (b) Evolution of C_{0x} with Q in cyclic loading with $t_Q = 4\tau$ (ω_Q/ω = 0.25). The closed blue curve A_sB_s in (b) is the steady-state hysteresis curve. $\eta = 1.0$, $L_p = 0.15$ and $\mu = 0.4$.

Fig. 9(b) is a plot of the evolution of horizontal approach C_{0x} as Q is cycled. In the first few Q cycles, the value of C_{0x} is large, but it decreases with additional cycling. Eventually, the system evolves into a closed, repeating loop, indicated by the blue curve $A_s - B_s$ in the figure. This is the steady-state hysteresis curve of the system. The area enclosed by this curve is a measure of the total amount of energy dissipated in a cycle because, as mentioned above, the contribution from the P load is relatively small. However, the enclosed area represents both viscous (pure hysteretic) and Coulomb losses.

In order to determine the viscous loss W_h, one utilizes the fact that in every load increment $dW_{ext} = dW_c + dW_h + dW_r$, and the change in the recoverable energy W_r over a steady-state cycle is 0. Thus,

$$W_h^{cycle} = W_{ext}^{cycle} - W_c^{cycle} \tag{4.6}$$

Since W_{ext}^{cycle} and W_c^{cycle} can be evaluated independently, this allows one to calculate W_h^{cycle}. Hysteresis curves for four different fretting analyses, with $t_Q = 0.2\tau, 1\tau, 2\tau$ and 4τ are shown in Fig. 10(a). It is clear that slower Q cycling rates (larger t_Q) correspond to larger energy losses per cycle. Fig. 10(b) shows that the viscous loss per cycle is the major component rather than the Coulomb loss, with a ratio of W_h/W_c of 1.9 at $t_Q = 0.2\tau$. This ratio increases to about 8.25 for $t_Q = 4\tau$.

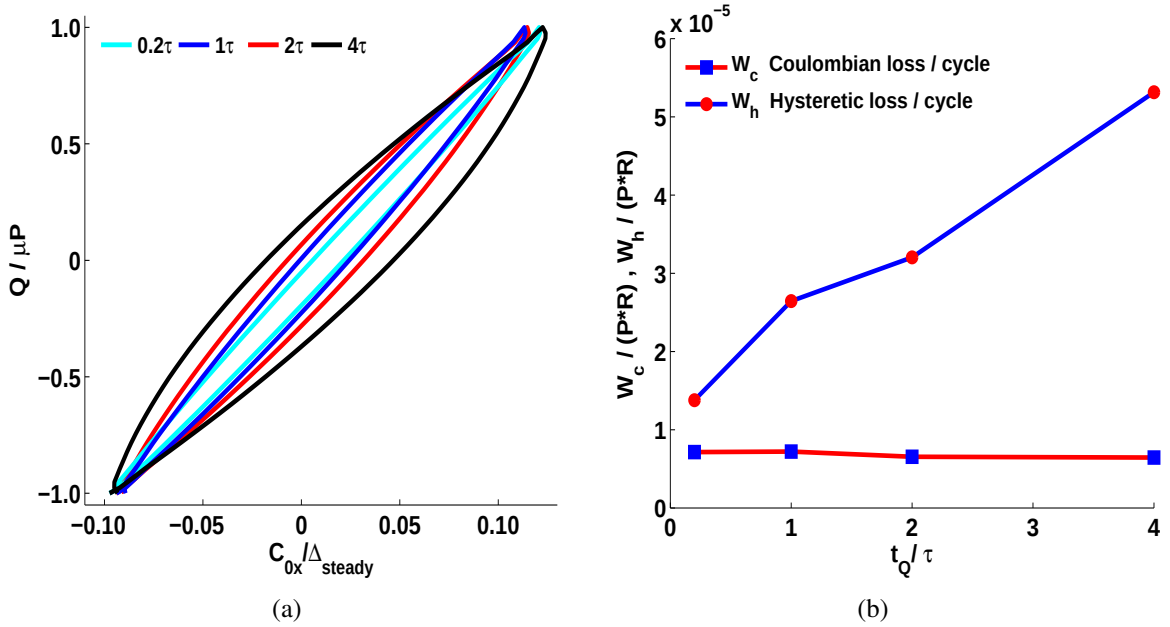

(a) (b)

Figure 10: (a) Hysteresis curves for fretting type loads for different Q-load cycle times t_Q and (b) The corresponding Coulomb and viscous losses per cycle. $\mu = 0.4$, $\eta = 1.0$, $L_p = 0.15$ in all cases. These load cycle times correspond to normalized loading frequencies ω_Q/ω = 5, 1, 0.5 and 0.25 respectively.The curves in (a) include contributions from both viscous and Coulomb losses, but, as shown in (b), the viscous losses are always larger than the Coulomb losses.

4.6. Slowly relaxing materials with multiple characteristic times

The SIE technique was also tested on an experimentally well-characterized polymer, Polymethyl methacrylate (PMMA), using a more representative 12-element viscoelastic network (Fig. 1b) with material data taken from Park and Schapery (1999). The relaxation function $\boldsymbol{G}(t)$ of this material is shown in Fig. 11(a). In contrast to the other two viscoelastic solids used in this paper, the PMMA has a very large ratio $G_0/G_\infty \sim 1000$.

Pressure and shear tractions for the 12-element PMMA for a ramp load-hold analysis are shown in Fig. 11(b). The P load is applied over 5s and then held constant. It is interesting to note that while the $N(\theta)$ relaxes with time just as for the three-element solid in Fig. 3(a), the tractions are far from steady even after a 150 sec hold. In fact, the rate at which $N(\theta)$ approaches the expected steady-state limit (indicated by the dashed blue line, corresponding to the elastic curve with G_∞) becomes exceedingly slow. This slow relaxation is due to the presence of very long time scales in this material, so that 'near-steady' conditions are not likely to be attained until $t \sim 10^7$ sec. In fact, even at t=400s (Fig. 11(a)), $\boldsymbol{G}(t) \sim 0.1G_0$, whereas $G_\infty \sim 0.001G_0$. This means that in fretting or other cyclic analyses, the material is *effectively* always in a transient state.

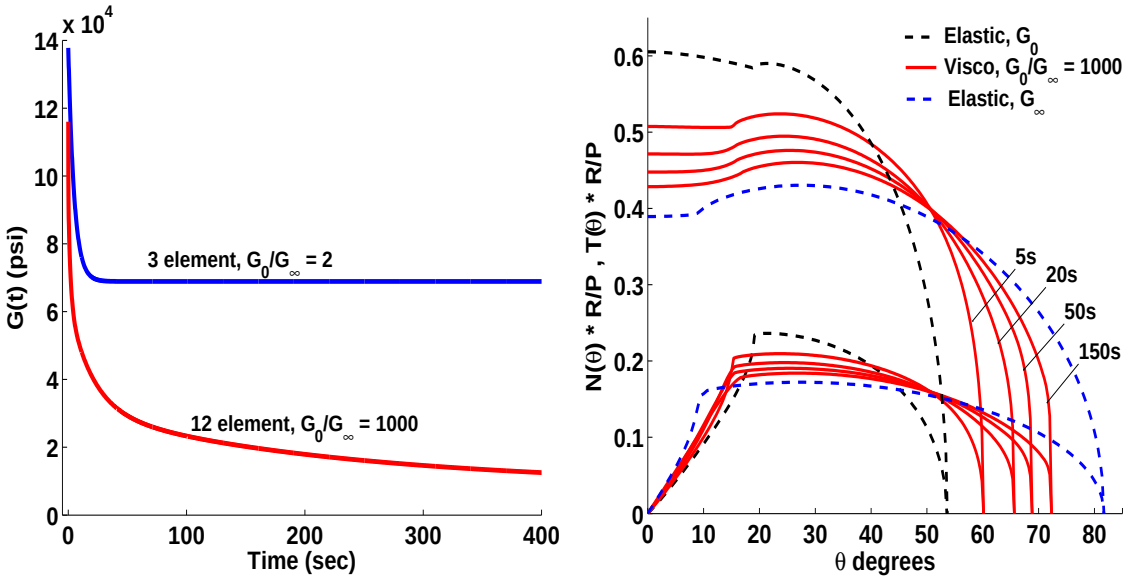

(a) (b)

Figure 11: (a) Relaxation functions $\boldsymbol{G}(t)$ for the two materials used in this paper. (b) Tractions in a P ramp load-hold analysis for a 12-element generalized Maxwell model for PMMA (Park and Schapery, 1999), with limiting (G_0, G_∞) elastic tractions superimposed. This material has very long time scales, and $G_0/G_\infty \sim 1000$, and would take a very long time to reach steady-state (blue dashed line).

5. Discussion

5.1. Correspondence principle in viscoelastic contact formulation

It is important to note that while the derivation of the viscoelastic Green's functions in Appendix A is equivalent to the use of a correspondence principle, the formulation of the contact problem itself (Sec. 2.2) does not use correspondence of any kind. In fact, despite the apparent algebraic similarity (see Sundaram and Farris (2010a)), the presence of the additional gap history terms in Eqs. (3.2), (3.3) renders the governing viscoelastic equations qualitatively different from their elastic counterparts. Thus, the viscoelastic contact problem is not reduced to an equivalent elastic one to solve it.

In addition, it is difficult to use integral transform techniques to solve fully-coupled partial slip problems because of the complicated nature of the boundary conditions and interaction between coulomb and viscous history effects; the 'direct' approach used in the present work seems to be the only feasible way.

5.2. Shakedown and steady state

As seen in section 4.6, materials with multiple, long relaxation time scales like the 12-element PMMA effectively never attain steady-state for reasonable testing times. This has several interesting implications. For instance, one has ever shifting edge-of-contact locations in the transient regime, and the concomitant edge-of-contact stresses occur at different locations over time. There

is no such issue for the three-element solid in Fig. 8, where the transients disappear fairly quickly; but it is significant for materials with long time scales. The lack of a steady 'edge-of-contact' and accompanying contact-shift probably results in 'smearing' of damage during load cycling. In addition, for such materials, the evolution of the $Q - C_{ox}$ curves in cyclic / fretting-type loading occurs very slowly (i.e. over a very large number of load cycles), rather than at the more rapid rate shown in Fig. 9(b) for a material with shorter time-scales. In this case, the calculation of a steady-state 'per-cycle' viscous loss using Eq. (4.6) is not possible.

Lastly, there is likely to be a qualitative change in the nature of the contact when one considers materials with very large values of G_0/G_∞. This is because the Coulomb model assumes incomplete (asperity) type contact, but with the relaxation of $\boldsymbol{G}(t)$ into the range associated with long-term elastomer moduli ($\leq$1 MPa), the contact is likely to become complete under loading (Persson et al., 2004), and thus cease to behave in a Coulombian manner.

5.3. Viscoelastic, elastic and FEA fretting tractions

In P-load hold analyses, the steady-state viscoelastic tractions agree very well with the elastic tractions using $G = G_\infty$, as seen in Figs. 3(a),3(b). This is because the contact patch increases in sizes monotonically. However, for cyclic / fretting loads, this is not true for typical Q-load cycling frequencies : It is then important to perform a viscoelastic analysis, rather than an approximate, elastic one. This can be seen in Figs. 12(a),12(b), where steady-state viscoelastic and elastic fretting tractions are compared for the three-element solid. The elastic analysis uses $G = G_\infty$. While the peak $N(\theta)$ are not very different in Fig. 12(a), there is a visible difference in the location of the ends of contact in steady-state, the difference being about $6^\circ - 7^\circ$. A more significant difference is observed in the shear tractions $T(\theta)$, as seen in Fig. 12(b). The implication is that a pure elastic analyses would identify the edge-of-contact incorrectly, by several degrees, which is quite significant. Further, the considerable difference in $T(\theta)$ leads to quite different edge-of-contact stresses. Of course, these effects would be accentuated for materials with long time-scales. For the same set of parameters, SIE fretting tractions were compared with tractions obtained using the ABAQUS / Standard FEA solver. A custom meshmaker was used to generate a mesh of 4-noded plane-strain elements with reduced integration, with $\sim$125 elements in contact. The FEA tractions are shown using markers in Figs. 12(a) and 12(b). There is good agreement between the FEA and SIE contact sizes and tractions. Surface stresses from the SIE technique are more accurate because one can directly calculate $\tilde{\sigma}_{\theta\theta}(\theta)$ using Eqs. (4.2). In FEA, these stresses are calculated at the nearest element Gauss quadrature point, which is sub-surface, and considerable mesh-refinement is required to obtain converged stresses.

It is also instructive to consider viscoelastic shakedown for non-typical Q-load cycle times, i.e., extremely low and high values of the normalized loading frequency ω_Q/ω. Intuitively, one might expect the shakedown tractions attained for small ω_Q/ω to be similar to those for an elastic material with long-term modulus G_∞. One might also expect the viscoelastic large ω_Q/ω and elastic G_0 cases to be similar. Fig. 13(a) shows the viscoelastic shakedown shear tractions obtained for

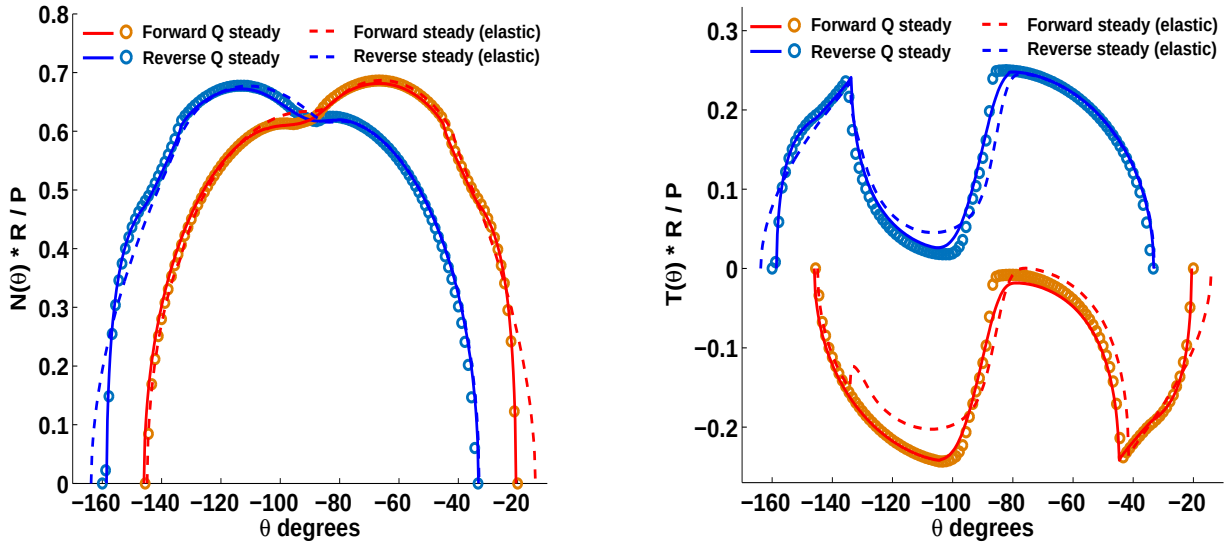

(a) (b)

Figure 12: (a) Pressure and (b) shear tractions for a fretting analysis comparing viscoelastic SIE (solid lines), elastic SIE (dashed lines) and viscoelastic FEA (circles) with identical parameters $\eta = 1.0$, $\mu = 0.4$, $t_Q/\tau = 2$ ($\omega_Q/\omega = 0.5$).

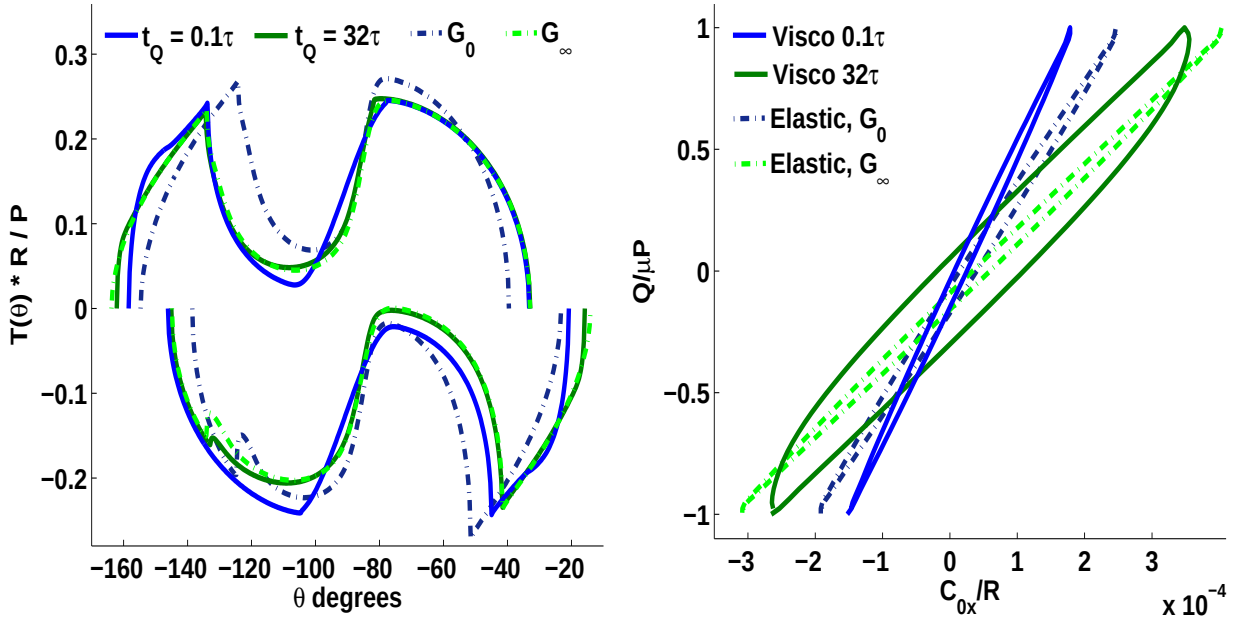

(a) (b)

Figure 13: (a) Shakedown shear tractions in fretting with high frequency ($\omega_Q/\omega = 10$, $t_Q/\tau = 0.1$) and low frequency ($\omega_Q/\omega = 0.03125$, $t_Q/\tau = 32$) load cycling in viscoelasticity, and limiting moduli (G_0, G_∞) in elasticity. (b) Hysteresis curves for these four analyses. Note that for elastic analyses, dissipation is entirely on account of coulomb friction. In all cases, $\eta = 1.0$, $L_p = 0.15$ and $\mu = 0.4$.

very low frequency loading (ω_Q/ω = 0.03125), high frequency loading (ω_Q/ω = 10), and elastic shakedown tractions using moduli G_0 and G_∞. It is clear that low frequency tractions agree quite well with the elastic G_∞ tractions. However, when ω_Q/ω = 10 (t_Q/τ = 0.1), the elastic (G_0) and viscoelastic tractions are quite different. This difference should, of course, diminish at even higher values of ω_Q/ω. Unfortunately, since the number of cycles to reach shakedown increases with increasing ω_Q/ω, probing even higher frequencies (e.g. ω_Q/ω = 50) seems to be currently infeasible by the SIE method, or indeed even by FEM, where the number of required analysis steps is similarly very large. Notably, Fig. 13(b) shows that the energy dissipated per cycle in slow cycling (ω_Q/ω = 0.03125) is significantly different from the elastic G_∞ case, even though the tractions are similar. From these results and our discussion above, one may conclude that for a fairly wide range of cyclic loading frequencies, it is essential to perform a viscoelastic analysis to obtain an accurate solution.

5.4. Coulomb and viscous history effects

Although both Coulomb friction and viscoelasticity contribute to the history effect, there are important differences between them. Viscoelastic material history transmission has an in-built 'fading memory effect', with recent times influencing the instantaneous solution more strongly than earlier times. This is because the relaxation function $\boldsymbol{G}(t)$ is a monotonically decreasing function, as seen in Fig. 11(a). In Coulomb friction, the transmission of history occurs in the stick-zone through Eq. (2.12). It is seen that slip history is transmitted exactly, with no 'fading' effect at all. However, unlike viscous history, there is a history erasure mechanism: The advance of slip zones into regions that were previously in stick.

Similarly, it is clear that in cyclic loading, viscous energy dissipation W_h^{cycle} typically dominates the Coulomb dissipation, as shown in Fig. 10(b). Possible offsetting factors, such as the use of higher values of μ do not change this result qualitatively. Moreover, recent experimental estimates of μ in stainless steel-PMMA contacts suggest that μ does not exceed ~ 0.65 even after numerous fretting cycles (Kim et al., 2013).

There are two possible explanations for the dominant role of viscous dissipation in viscoelastic partial slip contacts: The fact that material hysteresis is a bulk effect rather than a purely interfacial effect like Coulomb friction, and the generally limited slip amplitudes in geometrically conforming contacts. However, it is important to note that accurate *stress field* calculations require both effects to be considered; μ cannot be neglected.

6. Conclusion

This paper examines partial-slip fretting contacts in linear viscoelasticity. The governing equations were formulated as a pair of coupled Singular Integral Equations (SIEs) for a conforming (pin-plate) geometry, allowing Coulomb and hysteretic effects, general load histories and remote plate stresses. Viscoelasticity makes it necessary to apply the stick-zone boundary condition

in convolved form, and contributes additional convolved gap terms to the governing equations. Steady-state and transient tractions, as well as contact parameters, were studied under monotonic ramp-hold, unload-reload and cyclic bidirectional (fretting) loads for a three-element solid. While viscoelastic fretting contacts shakedown like elastic contacts, the number of cycles to do so is dependent on the ratio of the load cycle time to the relaxation time. Steady-state cyclic viscous dissipation typically dominates the cyclic Coulomb dissipation, with a more pronounced difference at slower load cycling. However, it is essential to include Coulomb friction for accurate contact stress analysis. Viscoelastic shakedown fretting tractions differ considerably from their (approximate) elastic counterparts for typical load cycling frequencies, highlighting the importance of viscoelastic analyses in cases where the contact patch is not monotonically increasing. In materials with very long time-scales, the material is effectively always in a transient state, with no steady edge-of-contact. This has implications for accumulated damage during fretting. Tractions obtained using SIE and FEA showed good agreement.

Acknowledgment

This work was supported in part by an Indian Space Research Organization(ISRO) / IISc Space Technology Cell research grant ISTC/CCE/NKS/335. The authors thank Professor S. Chandrasekar and Dr. K. Viswanathan of Purdue University for several helpful discussions on polymer interfaces.

APPENDIX : Green's functions

The Kolosov-Mushkelishvili formulation for a viscoelastic solid with time-independent Kolosov constant κ is (Golden and Graham, 1988)

$$\sigma_{rr} + \sigma_{\theta\theta} = 2\left(\Omega'(z;t) + \overline{\Omega'(z;t)}\right) \tag{A.1a}$$

$$\sigma_{rr} + i\sigma_{r\theta} = \Omega'(z;t) + \overline{\Omega'(z;t)} - \left(\bar{z}\,\overline{\Omega''(z;t)} + \frac{\overline{z}}{z}\,\overline{\omega'(z;t)}\right) \tag{A.1b}$$

$$2\int_{0^-}^{t^+} (v_r + iv_\theta)\boldsymbol{\mu^g}(t-\tau)d\tau = e^{-i\theta}\left\{\kappa\Omega(z;t) - z\,\overline{\Omega'(z;t)} - \overline{\omega(z;t)}\right\} \tag{A.1c}$$

$\boldsymbol{\mu^g}$ (and its inverse, $\boldsymbol{\gamma^g}$) are defined in terms of $\boldsymbol{G}$, $\boldsymbol{J}$ and the Heaviside step function $\mathcal{H}$ as follows

$$\boldsymbol{\mu^g}(t-\tau) = -\frac{d}{d\tau}\left[\mathcal{H}(t-\tau)\boldsymbol{G}(t-\tau)\right] \tag{A.2a}$$

$$\boldsymbol{\gamma^g}(t-\tau) = -\frac{d}{d\tau}\left[\mathcal{H}(t-\tau)\boldsymbol{J}(t-\tau)\right] \tag{A.2b}$$

For a traction b.v.p, a single-valued $F(\rho)$ is used to specify the boundary condition

$$\Omega(\rho;t) + \rho\,\overline{\Omega'(\rho;t)} + \overline{\omega(\rho;t)} = iF(\rho;t) \tag{A.3}$$

Consider the *elastic* problem for a point normal load N applied at an angular location $\xi = 0$ on the edge of a hole of radius R in an infinite plate. The following Kolosov potentials (Sundaram and Farris, 2010a; Rothman, 1950) solve this problem:

$$\Omega(z) = \frac{N}{2\pi}\left(-\log(z-R) + \frac{\kappa\log(z)}{(\kappa+1)}\right) \tag{A.4a}$$

$$\omega(z) = \frac{N}{2\pi}\left(\log(z-R) + \frac{z}{z-R} - \frac{\log(z)}{\kappa+1} - \frac{R}{z} - \frac{\kappa R^2}{(\kappa+1)}\frac{1}{z^2}\right) \tag{A.4b}$$

Now consider the analogous viscoelastic problem. It is clear from Eqs. (A.1a), (A.1b) and (A.3) that in this case, the viscoelastic potentials have no dependence on $\boldsymbol{\mu^g}$ and are of the form $\Omega(z;t) = N(t)g(z)$, where $g(z)$ is identical to the bracketed terms in the elastic case Eqs. (A.4a), (A.4b).

The left hand side of Eq. (A.1c) contains convolved displacements $\boldsymbol{\mu^g} * (v_r + iv_\theta)$. However, the right-hand side of Eq. (A.1c) has the same form as its elastic counterpart (England, 1971). Thus, the *convolved* surface displacements caused by point loads on the boundary of the viscoelastic plate are identical in form to the elastic surface displacements in Sundaram and Farris (2010a), with convolution replacing the elastic shear modulus G. For a compressive normal point load $N(t)$ applied at an angular location ξ, the radial and tangential surface displacements $\tilde{v}_r^N, \tilde{v}_\theta^N$ are

$$\int_{0^-}^{t^+} \left\{\tilde{v}_r^N \qquad \tilde{v}_\theta^N\right\} \boldsymbol{\mu^g}(t-\tau)d\tau = \frac{N(t)}{4\pi}\left\{\kappa'' SA - \kappa' CL \qquad \kappa' SL + \kappa'' CA\right\} \tag{A.5}$$

where $\kappa' = (\kappa+1)/2$, $\kappa'' = (\kappa-1)$, and the following spatial functions are introduced for the sake of brevity:

$$C \equiv C(\theta,\xi) \equiv \cos(\theta-\xi) \qquad A \equiv A(\theta,\xi) \equiv \frac{\theta-\xi}{2} - \frac{\pi}{2}\operatorname{sign}(\theta-\xi) \tag{A.6}$$

$$S \equiv S(\theta,\xi) \equiv \sin(\theta-\xi) \qquad L \equiv L(\theta,\xi) \equiv \log(2-2\cos(\theta-\xi)) \tag{A.7}$$

Similarly, for a tangential point load $T(t)$ acting at an angular location ξ on the edge of the hole,

$$\int_{0^-}^{t^+} \left\{\tilde{v}_r^T \qquad \tilde{v}_\theta^T\right\} \boldsymbol{\mu^g}(t-\tau)d\tau = \frac{T(t)}{4\pi}\left\{\kappa'' CA + \kappa' SL \qquad \kappa' CL - \kappa'' SA\right\} \tag{A.8}$$

To obtain the surface displacements, one convolves both sides of Eqs. (A.5),(A.8) with the linear

operator $\boldsymbol{\gamma^g}$, the inverse of $\boldsymbol{\mu^g}$. Since $\boldsymbol{\gamma^g} * \boldsymbol{\mu^g} = \delta(t)$ by definition,

$$\left\{\tilde{v}_r^N \qquad \tilde{v}_\theta^N\right\} = \frac{(\boldsymbol{\gamma^g} * N)(t)}{4\pi}\left\{\kappa'' SA - \kappa' CL \qquad \kappa' SL + \kappa'' CA\right\} \tag{A.9a}$$

$$\left\{\tilde{v}_r^T \qquad \tilde{v}_\theta^T\right\} = \frac{(\boldsymbol{\gamma^g} * T)(t)}{4\pi}\left\{\kappa'' CA + \kappa' SL \qquad \kappa' CL - \kappa'' SA\right\} \tag{A.9b}$$

It is useful to introduce the notation N^* and T^* respectively for the $\boldsymbol{\gamma^g}$-convolved N and T, e.g. $N^* \equiv \boldsymbol{\gamma^g} * N$. For remote stresses applied to the viscoelastic plate, the surface displacements are given by

$$\left\{\tilde{v}_r^\infty \qquad \tilde{v}_\theta^\infty\right\} = \frac{R\kappa^{'}}{2}\left\{\frac{\mathscr{A}^*}{2} + \mathscr{D}^*\cos(2\theta) \qquad -\mathscr{D}^*\sin(2\theta)\right\} \tag{A.10}$$

where $\mathscr{A}^* \equiv \boldsymbol{\gamma^g} * \mathscr{A}(t) = \boldsymbol{\gamma^g} * (\sigma_{xx}^\infty(t) + \sigma_{yy}^\infty(t))$, $\mathscr{D}^* \equiv \boldsymbol{\gamma^g} * \mathscr{D}(t) = \boldsymbol{\gamma^g} * (\sigma_{xx}^\infty(t) - \sigma_{yy}^\infty(t))$.

References

Barber, J., 2010. Elasticity, 3rd Edition. Solid Mechanics and its Applications. Springer Science, New York.

Carbone, G., Putignano, C., 2013. A novel methodology to predict sliding and rolling friction of viscoelastic materials: Theory and experiments. Journal of the Mechanics and Physics of Solids 61 (8), 1822–1834.

Chen, W. W., Wang, Q. J., Huan, Z., Luo, X., 2011. Semi-analytical viscoelastic contact modeling of polymer-based materials. Journal of Tribology 133 (4), 041404.

Duisabeau, L., Combrade, P., Forest, B., 2004. Environmental effect on fretting of metallic materials for orthopaedic implants. Wear 256 (7), 805–816.

Dundurs, J., Comninou, M., 1979. Some consequences of the inequality conditions in contact and crack problems. Journal of Elasticity 9 (1), 71–82.

England, A. H., 1971. Complex variable methods in elasticity. Dover Publications, New York, USA.

Fellows, L., Nowell, D., Hills, D., 1995. Contact stresses in a moderately thin strip (with particular reference to fretting experiments). Wear 185 (1), 235–238.

Geringer, J., Forest, B., Combrade, P., 2005. Fretting-corrosion of materials used as orthopaedic implants. Wear 259 (7), 943–951.

Gladwell, G., 1980. Contact Problems in the Classical Theory of Elasticity. Monographs and Textbooks on Mechanics of Solids and Fluids. Sijthoff and Noordhoff, The Netherlands.

Golden, J. M., Graham, G. A. C., 1988. Boundary value problems in linear viscoelasticity. Springer.

Golden, J. M., Graham, G. A. C., 2001. Viscoelastic inclusion i: Partial contact under bi-directional loading. Zeitschrift für angewandte Mathematik und Physik ZAMP 52 (3), 357–396.

Goodman, L., 1962. Contact stress analysis of normally loaded rough spheres. Journal of applied mechanics 29 (3), 515–522.

Goryacheva, I., 1973. Contact problem of rolling of a viscoelastic cylinder on a base of the same material: Pmm vol. 37, n 5, 1973, pp. 925–933. Journal of Applied Mathematics and Mechanics 37 (5), 877–885.

Goryacheva, I., 2008. Viscoelasticity, wear and roughness. In: Galin, L. A., Gladwell, G. M. L. (Eds.), Contact problems: the legacy of LA Galin. Springer Science & Business Media, New York, pp. 153–197.

Goryacheva, I., Sadeghi, F., 1995. Contact characteristics of a rolling/sliding cylinder and a viscoelastic layer bonded to an elastic substrate. Wear 184 (2), 125–132.

Graham, G., 1967. The contact problem in the linear theory of viscoelasticity when the time dependent contact area has any number of maxima and minima. International Journal of Engineering Science 5 (6), 495–514.

Grosch, K., 1963. The relation between the friction and visco-elastic properties of rubber. Proceedings of the Royal Society of London A: Mathematical, Physical and Engineering Sciences 274 (1356), 21–39.

Higham, P., Stott, F., Bethune, B., 1978. Mechanisms of wear of the metal surface during fretting corrosion of steel on polymers. Corrosion Science 18 (1), 3–13.

Hills, D., Nowell, D., 1994. Mechanics of Fretting Fatigue. Vol. 30 of Solid Mechanics and its Applications. Kluwer Academic Publishers, The Netherlands.

Hui, C.-Y., Baney, J., Kramer, E., 1998. Contact mechanics and adhesion of viscoelastic spheres. Langmuir 14 (22), 6570–6578.

Hunter, S., 1961. The rolling contact of a rigid cylinder with a viscoelastic half space. Journal of Applied Mechanics 28 (4), 611–617.

Hunter, S. C., 1960. The hertz problem for a rigid spherical indenter and a viscoelastic half-space. Journal of the Mechanics and Physics of Solids 8 (4), 219–234.

Johnson, K. L., 1987. Contact mechanics. Cambridge university press.

Kalker, J. J., 1991. Viscoelastic multilayered cylinders rolling with dry friction. Journal of applied mechanics 58 (3), 666–679.

Kim, K., Geringer, J., Pellier, J., Macdonald, D. D., 2013. Fretting corrosion damage of total hip prosthesis: Friction coefficient and damage rate constant approach. Tribology International 60, 10–18.

Lee, E. H., Radok, J. R. M., 1960. The contact problem for viscoelastic bodies. Journal of Applied Mechanics 27 (3), 438–444.

Margetson, J., Morland, L., 1970. Separation of smooth circular inclusions from elastic and viscoelastic plates subjected to uniaxial tension. Journal of the Mechanics and Physics of Solids 18 (4), 295–309.

McVeigh, P., Harish, G., Farris, T., Szolwinski, M., 1999. Modeling interfacial conditions in nominally flat contacts for application to fretting fatigue of turbine engine components. International Journal of Fatigue 21, S157–S165.

Morland, L., 1968. Rolling contact between dissimilar viscoelastic cylinders. The Quarterly Journal of Mechanics and Applied Mathematics 25 (4), 363–376.

Muskhelishvili, N., 1992. Singular Integral Equations. Dover Books on Mathematics. Dover Publications, Inc., The United States of America.

Park, S., Schapery, R., 1999. Methods of interconversion between linear viscoelastic material functions. part ia numerical method based on prony series. International Journal of Solids and Structures 36 (11), 1653–1675.

Persson, B., Albohr, O., Creton, C., Peveri, V., 2004. Contact area between a viscoelastic solid and a hard, randomly rough, substrate. The Journal of chemical physics 120 (18), 8779–8793.

Persson, B. N., 2001. Theory of rubber friction and contact mechanics. The Journal of Chemical Physics 115 (8), 3840–3861.

Rothman, M., 1950. Isolated force problems in two-dimensional elasticity (i). Quarterly Journal of Mechanics and Applied Mathematics 3, 279–296.

Sternberg, E., Al-Khozaie, S., 1964. On green's functions and saint-venant's principle in the linear theory of viscoelasticity. Archive for Rational Mechanics and Analysis 15 (2), 112–146.

Sundaram, N., Farris, T. N., 2010a. The generalized advancing conformal contact problem with friction, pin loads and remote loading–case of rigid pin. International Journal of Solids and Structures 47 (6), 801–815.

Sundaram, N., Farris, T. N., 2010b. Mechanics of advancing pin-loaded contacts with friction. Journal of the Mechanics and Physics of Solids 58 (11), 1819–1833.

Ting, T. C. T., 1966. The contact stresses between a rigid indenter and a viscoelastic half-space. Journal of Applied Mechanics 33 (4), 845–854.

To, Q., He, Q.-C., 2008. On the conforming contact problem in a reinforced pin-loaded structure with a non-zero second dundurs constant. International Journal of Solids and Structures 45 (14), 3935–3950.

Tritschler, B., Forest, B., Rieu, J., 1999. Fretting corrosion of materials for orthopaedic implants: a study of a metal/polymer contact in an artificial physiological medium. Tribology international 32 (10), 587–596.